Measurement of High-Frequency Milling Forces with Dynamic Compensation

by

Alan Jullien-Corrigan
B.Eng, University of Victoria, 2019

A Report Submitted in Partial Fulfillment of the
Requirements for the Degree of

MASTER OF ENGINEERING

in the Department of Mechanical Engineering

Measurement of High-Frequency Milling Forces with Dynamic Compensation

by

Alan Jullien-Corrigan
B.Eng, University of Victoria, 2019

Supervisory Committee

Dr. Keivan Ahmadi, Supervisor
(Department of Mechanical Engineering)

Dr. Joshua Giles, Departmental Member
(Department of Mechanical Engineering)

Dr. Mohsen Akbari, Chair
(Department of Mechanical Engineering)

ABSTRACT

Piezoelectric dynamometers are widely used to measure cutting forces during milling operations for diagnostic, process monitoring, and research and development purposes. However, the bandwidth of tooth passing frequencies that can be measured has an upper limit due to the electromechanical dynamics of the measurement device. As a result, high-frequency forces cannot be accurately measured. Even if an effort is made to match the cutting conditions to the specifications of the dynamometer, the higher harmonics of the tooth-passing frequency are still affected so that the resulting measurements are distorted.

In this work, two new (for milling applications) methods are presented to reconstruct the machining forces from the distorted measurement signal and compared to an existing method, the Augmented Kalman Filter (AKF). The first method implements a Sliding Mode Observer (SMO) to estimate the machining forces at each time-step from the measured signal. The second method, referred to as Regularized Deconvolution (RD), considers the convolution sum of the input machining force and the impulse response of the system, and then reconstructs the machining force signal by regularizing a related inverse problem. All three methods are implemented in a simulation study that imitates the cutting conditions used in a latter experimental cutting test in which the above methods are again used to recover the true machining forces and their relative performance evaluated and compared. A transfer function model of the electomechanical dynamics of a Kistler dynamometer is identified and incorporated into the simulation study and the experiment.

The results of this work find that, while all three methods reconstruct the true machining forces reasonably well, SMO has clear advantages for processes carried out over time in which the system dynamics changes. AKF also performs better than RD, but is not robust against variations in system dynamics. Despite its drawbacks, RD does have the advantage of being the method that only requires one parameter to be tuned, whereas the other methods require the tuning of two or more parameters.

Contents

List of Tables

List of Figures

ACRONYMS

AKF Augmented Kalman Filter

CNC Computer Numerical Control

FFT Fast Fourier Transform

FRF Frequency Response Function

NRMSE Normalized Root Mean Square Error

RD Regularized Deconvolution

SMO Sliding Mode Observer

SNR Signal to Noise Ratio

VSCS Variable Structure Control System

ACKNOWLEDGEMENTS

I would like to express my deepest thanks to all of the members of the Dynamics and Digital Manufacturing Laboratory at the University of Victoria for creating a congenial work environment and for making my time at UVic unforgettable. I would like to thank in particular Yaser Mohammadi and Han Chen for being generous with both their time and technical expertise; Mehran Farhadmanesh for his advice and guidance; and Kashif Nadeem, Xi Wang, and Shuan Cook for their friendship and camaraderie. And of course, I owe the greatest debt of gratitude to my supervisor Dr. Keivan Ahmadi for his support, mentorship, and patience. His professionalism, enthusiasm for the subject matter, and rigour is a model of excellence I will not soon forget.

Chapter 1

Introduction

1.1 Background

The determination of machining forces is an important part of process monitoring and quality control in manufacturing processes[1, 2, 3], allowing for the optimization of tool life and process time while ensuring an acceptable surface finish on the workpiece. The machining forces are often measured directly to ensure that the reported quantities are as accurate as possible. Two common measurement devices used for this purpose are accelerometers and dynamometers. Accelerometers consist of piezoelectric sensors that are attached at strategic locations to sense the acceleration components imparted onto the workpiece by the machining process. Dynamometers, which are far more popular and widely used, consist of piezoelectric load cells arranged and packaged in a mechanical structure that detects the Cartesian components of the machining forces applied by the tool. However, the force measurement provided by the dynamometer is adversely affected by the stiffness and inertia of the structural elements in the load path between the tool and the load cells, as the dynamometer is often incorporated as part of a fixture assembly for the workpiece. A typical arrangement is shown in Fig.1.1. The resulting measurement error is further compounded by the electrical dynamics of the dynamometer, which limits the bandwidth at which machining forces can be reliably measured. However, machining forces are periodic at the frequency with which the cutting edge passes through the workpiece, and as a result the force components represented by higher harmonics may still be distorted despite attempts to match the spindle frequency to the specifications of the dynamometer. The corresponding measurement error can result in sub-optimal

process time, unacceptable surface finishes, shorter tool life, and even catastrophic failure and increased downtime in certain situations.

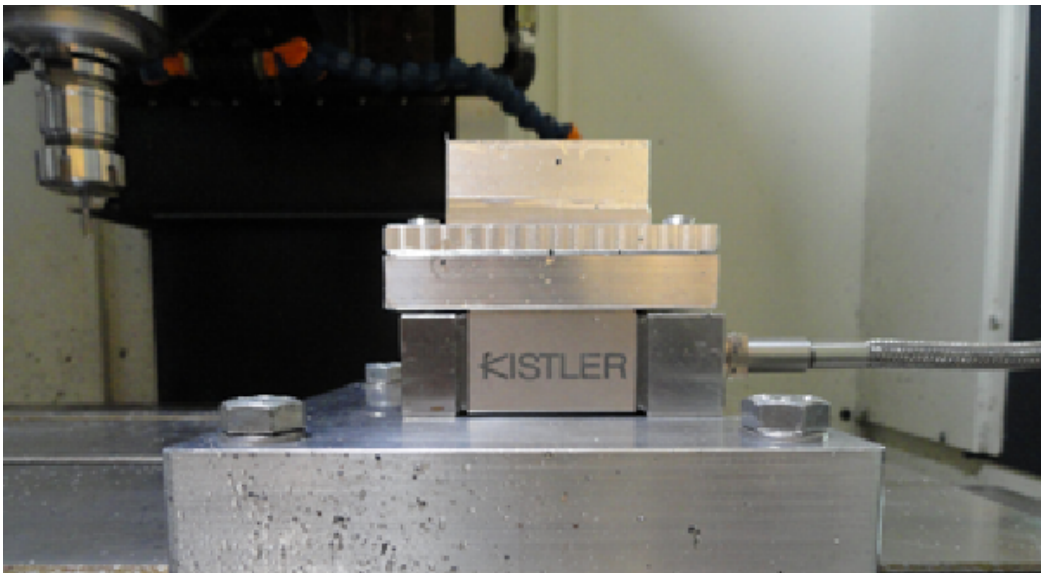

Figure 1.1: The system consists of the workpiece that interacts with the cutting tool and the piezoelectric sensors in the dynamometer and the structural link connecting it to the workpiece.

1.2 Literature Review and Project Objectives

A number of techniques, in both the time[4] and frequency[5] domain, have been proposed to estimate machining forces. Many online methods involve designing and implementing an observer. An observer uses known information about a system and its inputs to estimate the output and evolving states of the system. The estimated outputs are compared to the actual outputs of the system to provide feedback to the observer so that the estimation error will converge to a minimum, if not eliminated completely. While observers have been traditionally used to estimate states, these structures have more recently been expanded to estimate both states and forces. Alcocer [6] built upon a classical observer for linear systems to estimate external ramp forces resulting from the interaction between a serially linked robot and its environment. Mohammadi [7] proposed a design method, formulated as solving a linear matrix inequality, for a general disturbance torque observer for serial-linked robots regardless of the number and type of actuators and the configuration of the end-effector. However, the observer employed by both Alcocer and Mohammadi exhibits

minor tracking errors and requires a compromise between the rate of observer convergence and sensitivity to measurement noise.

Lourens [8] estimated unknown forces in a structural dynamics problem by using a deterministic-stochastic model in an Augmented Kalman Filter (AKF), where the state vector is augmented to include the unknown forces. The dual deterministic-stochastic model has the advantage of capturing modelling errors as well as the measurement uncertainty incorporated in classical Kalman Filters. AKF is able to identify unknown forces from co-located accelerometer measurements, although the performance of the filter falters when trying to identify distant forces. Further issues arise when trying to identify forces from spurious low-frequency content of the measurements. AKF and similar variations on the Kalman Filter, such as the extended active observer [9], have also been employed in the field of manufacturing.

Jacquelin [10] reconstructed an unknown force by deconvolving measurement signals from a structure's impulse response. Deconvolution, however, involves solving an ill-posed and computationally expensive inverse problem, requiring regularization as well as constraining the problem to include certain assumptions that may not match reality in some cases. These factors mean that deconvolution with regularization is often used as an offline method. Bai [11] estimated the forces and torques produced by muscles by using the continuous wavelet transform, an alternative to the short-time Fourier transform, and artificial neural networks, a tool commonly used to map the inputs and outputs of highly non-linear systems. Bai was able to demonstrate a strong correlation between the estimated forces and torques and those measured using electromyography. However, it is necessary to "train" the artificial neural network by providing it with calibration data, making the method unsuitable for handling disturbances and other forces that do not fit the mould of the training forces.

Mihoub [12] demonstrated the performance of a second-order discrete-time Sliding Mode Observer (SMO) and its suitability for online process control applications. This suitability and its characteristic robustness make sliding mode observers an attractive option for identifying forces in a dynamic environment, as in most manufacturing processes. However, this method has not yet been applied to estimating cutting forces during milling at the time of writing.

This work presents two new methods to estimate cutting forces during milling from dynamometer measurements and compares their performance to the AKF. The first method, SMO, models the dynamics of the dynamometer in the time domain as a state space model with the cutting forces cast as an input disturbance, which is estimated by the observer. The second method, Regularized Deconvolution (RD), considers the convolution sum of the (input) cutting forces and the impulse response of the system. The unknown forces are recovered from the inverse solution of the corresponding matrix equation, with a regularizing factor introduced to reduce noise magnification. In the first part of this work, the dynamics of the system shown in 1.1, which includes the dynamics of the dynamometer, will be identified and used as the basis of a simulation study of the three methods, in which simulated cutting forces will be recovered after being distorted by the identified dynamics. In the second part of this work, the three methods will be used to reconstruct the milling forces generated during an experimental cutting test conducted on the physical workpiece.

1.3 Report Outline

The content of this report is organized in the subsequent chapters as follows. The theoretical basis for SMO, AKF, and RD methods is given in chapter 2. Chapter 3 presents the identified dynamics of the dynamometer and the numerical simulations that verified the different methods, while the experimental procedure and results are treated by chapter 4. A summary of the results and concluding remarks are given in chapter 5.

Chapter 2

Background Theory

2.1 Augmented Kalman Filter

Any linear mechanical process, including milling, can be modelled by the following state space equations:

$$\begin{aligned} \dot{x} &= Ax + Bu \\ y &= Cx + Du \end{aligned} \tag{2.1}$$

where x is the state vector, u is the input vector, y is the output vector, A is the system matrix, B is the input matrix, C is the output matrix, and D is the feed-forward matrix. Introducing a zero-order hold and introducing process-specific variables for milling while neglecting the feed-forward matrix allows equation 2.1 to be expressed in the discrete-time domain:

$$\begin{aligned} \{x(k+1)\} &= [A_d]\{x(k)\} + \{B_d\}F_m(k) \\ F_d(k) &= [C]\{x(k)\} \end{aligned} \tag{2.2}$$

where $\cdot(k) = \cdot(k\Delta t)$, F_m and F_d are the true machining and dynamometer measured forces respectively, and

$$[A_d] = e^{A\Delta t}; \quad \{B_d\} = \int_0^{\Delta t} e^{A\Delta t}\{B\}dt \tag{2.3}$$

Stochastic processes can be considered by adding process ($w(k)$) and output ($v(k)$) noise terms to the state and output transition equations, respectively, in equation 2.2.

For such a system with the input vector u neglected, the unknown states can be determined by using the standard Kalman filter algorithm, which recursively estimates the state vector. The algorithm works by calculating a gain K, called the Kalman gain, that minimizes the state estimation covariance matrix, P. Then the Kalman gain is used to update the estimate for P and the state vector, which are projected ahead to the next time step. The process repeats iteratively until the estimated state vector and Kalman gain converge. Formally, the Kalman filter algorithm is given by[13]:
Measurement Update Stage:

$$\begin{aligned} K_k &= P_k^- H_k^T (H_k P_k^- H_k^T + R_k)^{-1} \\ \hat{x}_k &= \hat{x}_k^- + K_k(z_k - H_k \hat{x}_k^-) \\ P_k &= (I - K_k H_k) P_k^- \end{aligned} \tag{2.4}$$

Projection Stage:

$$\begin{aligned} \hat{x}_{k+1}^- &= \phi_k \hat{x}_k \\ P_{k+1}^- &= \phi_k P_k \phi_k^T + Q_k \end{aligned} \tag{2.5}$$

Here, Q is the process noise covariance matrix, H is the output matrix C from equations 2.1, ϕ is the state transition matrix (A from equations 2.1), and z is the output measurement y. $\hat{\cdot}$ denotes an estimated value, while $\cdot^-$ refers to a quantity in the current time step k prior to it being updated. To estimate the cutting forces represented by the input vector u, AKF can be implemented, as was done by Laurens et al., which supplements the state equations with an equation that models the time history of the unknown forces as[8]

$$p_{k+1} = p_k + \eta_k \tag{2.6}$$

so that the force vector p at the next time step is the force at the current time step plus a stochastic component η. The state vector is augmented to include the unknown force as a state variable. Then the state equations become [8]

$$\begin{aligned} x_{k+1}^a &= A_a x_k^a + \zeta_k \\ d_k &= G_a x_k^a + \upsilon_k \end{aligned} \tag{2.7}$$

with

$$\begin{aligned} x_k^a &= \begin{bmatrix} x_k \\ p_k \end{bmatrix} \\ A_a &= \begin{bmatrix} A & B \\ 0 & I \end{bmatrix} \\ G^a &= \begin{bmatrix} C & D \end{bmatrix} \\ \zeta_k &= \begin{Bmatrix} w_k \\ \eta_k \end{Bmatrix} \end{aligned} \tag{2.8}$$

where sub- and superscript 'a' stands for "augmented." The Kalman filter using the augmented state equations becomes [8]

Measurement Update Stage:

$$\begin{aligned} K_k &= P_k^- G_{a,k}^T (G_{a,k} P^- G_{a,k}^T + R_k)^{-1} \\ \hat{x}_k^a &= \hat{x}_k^{a,-} + K_k (d_k - G_{a,k} \hat{x}_k^{a,-}) \\ P_k &= (I - K_k G_{a,k}) P_k^- \end{aligned} \tag{2.9}$$

Projection Stage:

$$\begin{aligned} \hat{x}_{a,k+1}^- &= A_{a,k} \hat{x}_{a,k} \\ P_{k+1}^- &= A_k P_k A_k^T + Q_{a,k} \end{aligned} \tag{2.10}$$

with

$$Q_a = \begin{bmatrix} Q & 0 \\ 0 & S \end{bmatrix} \tag{2.11}$$

Here, S is a regularizing factor that regularizes noise magnification during force reconstruction. The choice of S represents a trade-off between the estimation error and the smoothness of the cutting forces. Choosing an optimal value of S is discussed in more detail in the next chapter.

2.2 Sliding Mode Observer Theory

Sliding Mode Control is based on the concept of Variable Structure Control Systems (VSCS), where the control law changes based on the state of the system. The motivation for such a system is to asymptotically drive the state vector to some stable equilibrium state x_e on the phase portrait irrespective of the specific dynamics of the system. This behaviour is achieved by introducing a sliding surface on the phase portrait and by judicious choice of gains for the control law, both of which are designed so that the sliding surface is in the vicinity of the desired equilibrium state and the state trajectory reaches the sliding surface in finite time. A switching function is implemented whereby the control action changes upon the state vector passing the sliding surface so that the state vector remains bound to the sliding surface. In this way, the control action consists of two stages: first, when the state approaches the sliding surface, and second, when the state is on the sliding surface asymptotically approaching equilibrium.

In this method, the above framework as presented by Edwards et al.[14] is used to design an observer that treats the machining forces in equation 2.1 as an input disturbance. The observer is defined as[14]

$$\{\dot{\hat{x}}(t)\} = [A]\{\hat{x}(t)\} - [G_l][C]\{e(t)\} + \{G_n\}\nu(t) \tag{2.12}$$

The unknown disturbance is compensated for by adding linear and nonlinear feedback loops, whose gains are $[G_l]$ and $[G_n]$, respectively, to the observer. The injection signal $\nu(t)$ is defined by the switching function[14]

$$\nu = \begin{cases} -\rho\frac{[C]\{e\}}{|[C]\{e\}|} & \text{if } [C]\{e\} \neq 0 \\ 0 & \text{otherwise} \end{cases} \tag{2.13}$$

where ρ is the gain of the switching function. $[G_l]$, $[G_n]$, and ρ are designed so that the state estimation error goes to zero asymptotically while the output estimation error, $[C]\{e(t)\}$, is bounded on the following sliding surface:

$$S_o = \{e \in \mathbb{R}^n : [C]\{e\} = 0\} \tag{2.14}$$

Equation 2.14 ensures that $[C]\{e\} \rightarrow 0$ in finite time. The necessary and sufficient conditions for the above observer to converge is that the system model be equivalent to a relative degree one transfer function with minimum phase. To design the feedback loop gains, coordinate transformations[14] are applied to equation 2.1 to cast the state space model in the following special canonical form:[14]

$$\begin{gathered} \left\{ \begin{array}{c} \dot{x}_1(t) \\ \dot{F}_d(t) \end{array} \right\} = \left[\begin{array}{cc} \mathcal{A}_{11} & \mathcal{A}_{12} \\ \mathcal{A}_{21} & \mathcal{A}_{22} \end{array} \right] \left\{ \begin{array}{c} x_1(t) \\ F_d(t) \end{array} \right\} + \left\{ \begin{array}{c} 0_{n-1} \\ \mathcal{B} \end{array} \right\} F_m(t) \\ F_d(t) = [\mathcal{C}] \left\{ \begin{array}{c} x_1(t) \\ F_d(t) \end{array} \right\} \end{gathered} \tag{2.15}$$

which is obtained from

$$\begin{gathered} \left[\begin{array}{cc} \mathcal{A}_{11} & \mathcal{A}_{12} \\ \mathcal{A}_{21} & \mathcal{A}_{22} \end{array} \right] = [T_b]\,[T_c]\,[A]\,[T_c]^{-1}\,[T_b]^{-1}\,; \\ \left\{ \begin{array}{c} 0_{n-1} \\ \mathcal{B} \end{array} \right\} = [T_b]\,[T_c]\,\{B\}; \\ [\mathcal{C}] = [C]\,[T_c]^{-1} = \left[\begin{array}{cc} 0_{n-1} & 1 \end{array} \right] \end{gathered} \tag{2.16}$$

where

$$[T_b] = \left[\begin{array}{cc} I_{n-1} & -B_c/B_c(n) \\ 0_{n-1} & 1 \end{array} \right]; \quad [T_c] = \left[\begin{array}{c} \text{Null}(C)^T \\ C \end{array} \right] \tag{2.17}$$

and $\{B_c\} = [T_c]\,\{B\}$, and $B_c(n)$ is the last element of the vector $\{B_c\}$. Defining the following observer for the special canonical system[14]

$$\begin{aligned} \{\dot{\hat{x}}_1(t)\} &= [\mathcal{A}_{11}]\,\{\hat{x}_1(t)\} + \mathcal{A}_{12}\hat{F}_d(t) - \mathcal{A}_{12}e_{fd}(t) \\ \dot{\hat{F}}_d(t) &= [\mathcal{A}_{21}]\,\{\hat{x}_1(t)\} + \mathcal{A}_{22}\hat{F}_d(t) - (\mathcal{A}_{22} - \mathcal{A}^s_{22})\,e_{fd}(t) + v \end{aligned} \tag{2.18}$$

and comparing the above with equation 2.12, it is observed that the linear and non-linear feedback gains are[14]

$$\begin{aligned} [G_l] &= [T_c]^{-1}[T_b]^{-1} \left[\begin{array}{c} \mathcal{A}_{12} \\ \mathcal{A}_{22} - A^s_{22} \end{array} \right] \\ [G_n] &= \mathcal{B}[T_c]^{-1}[T_b]^{-1} \left[\begin{array}{c} 0_{n-1} \\ 1 \end{array} \right] \end{aligned} \tag{2.19}$$

where A_{22}^s is any stable pole of the observer dynamics and $e_{fd} = \hat{F}_d(t) - F_d(t)$ is the estimation error of the output. After subtracting the state vector by its estimated variable, in equations 2.15 and 2.18 respectively, the estimation error dynamics are obtained as[14]

$$\{\dot{e}_1(t)\} = [\mathcal{A}_{11}]\{e_1(t)\} \tag{2.20}$$

$$\dot{e}_{fd}(t) = [\mathcal{A}_{21}]\{e_1(t)\} + \mathcal{A}_{22}^s e_{fd}(t) + v - \mathcal{B}F_m \tag{2.21}$$

where the state estimation error is $\{\dot{e}_1(t)\} = \{\hat{x}_1(t)\} - \{x_1(t)\}$. The previously mentioned condition of minimum phase guarantees the asymptotic stability of $\{e_1(t)\}$ as the system transfer function zeros and the eigenvalues of $[\mathcal{A}_{11}]$ are equivalent[14]. Furthermore, the condition that $\dot{e}_{fd}.e_{fd} < 0 \forall t$ can be ensured if the nonlinear injection signal is large enough, which is achieved if the switching gain is sufficiently high. This is the condition that sliding motion occurs, or in other words that the state trajectory on the phase portrait converges to the sliding surface, in finite time. Note that nothing has been said of the system under consideration except for the conditions of minimum phase and relative degree one; therefore, the observer is robust against the changing dynamics of the system.

It is readily observed from equation 2.21 that the milling forces are estimated by $\hat{F_m} = v/\mathcal{B}$ once sliding motion occurs and the state estimation error becomes negligible. However, the theoretically infinite frequency of the injection signal causes undesirable chattering behaviour in mechanical systems [14]. Therefore, the cutting forces are recovered from the smoothed switching function[14]

$$\hat{f}_m = \frac{-\rho}{\mathcal{B}} \frac{[C]\{e\}}{\delta + |[C]\{e\}|} \tag{2.22}$$

where δ is a positive constant that can be tuned to determine how much of the high-frequency content from the discontinuous injection signal is to be removed.

2.3 Regularized Deconvolution Theory

For the discrete-time system of equation 2.2, the convolution sum of the input cutting forces and the impulse response of the system, $h(k)$, yields the response of the

system[10]:

$$F_d(k) = \sum_{l=0}^{k} h(l) F_m(k-l) \tag{2.23}$$

The impulse response can be expressed as:

$$h(l) = 0 \quad \text{for} \quad l \leq 0, \quad \text{and} \quad h(l) = [C][A_d]^{l-1}[B_d] \quad \text{for} \quad l = 1, 2, ... \tag{2.24}$$

The following matrix equation relating the input cutting forces and the measured output forces is constructed by repeating equation 2.23 for N consecutive timesteps:

$$\begin{bmatrix} F_d(0) & F_d(1) & \cdots & F_d(N-1) \end{bmatrix}^T = [G] \begin{bmatrix} F_m(0) & F_m(1) & \cdots & F_m(N-1) \end{bmatrix}^T \tag{2.25}$$

$[G]$ is a Hankel matrix of the impulse responses at N timesteps with a lower triangular form:[10]

$$[G] = \begin{bmatrix} h(0) & 0 & \cdots & 0 \\ h(1) & h(0) & \cdots & 0 \\ \vdots & \vdots & \vdots & \vdots \\ h(N-1) & h(N-2) & \cdots & h(0) \end{bmatrix} \tag{2.26}$$

Using this framework, the true machining forces can be obtained from the inverse solution of equation 2.25. However, this has the undesirable effect of magnifying measurement and process noise as $[G]$ is ill-conditioned. This is rectified by employing the following regularized least squares estimation to obtain the unknown vector of machining forces: [10]:

$$\begin{Bmatrix} \hat{F_m}(0) \\ \hat{F_m}(1) \\ \vdots \\ \hat{F_m}(N-1) \end{Bmatrix} = \begin{bmatrix} G \\ \sqrt{\alpha} I_{N \times N} \end{bmatrix}^+ \begin{Bmatrix} \tilde{F_d}(0) \\ \tilde{F_d}(1) \\ \vdots \\ \tilde{F_d}(N-1) \\ 0_{N \times N} \end{Bmatrix} \tag{2.27}$$

where + signifies the pseudoinverse, and the regularization factor, α, is used to find an ideal trade-off between the noise magnification and the estimation error.

Chapter 3

Simulation Study

Some of the material presented in this chapter first appeared in "Measurement of high-frequency milling forces using piezoelectric dynamometers with dynamic compensation" Journal of Precision Engineering*, vol.66, pp.1-9,2020.*

In order to verify the methods outlined in the previous chapter, the system shown in Fig.1.1 must be identified. The frequency response function (FRF) of the system is determined by the application of successive hammer tests in the 3 coordinate axes of the CNC machine. Typical hammer tests consist of striking the system with an instrumented hammer and recording the system's response, typically with accelerometers. The frequency response function is then constructed from the measured impulse response of the system and the force data from the instrumented hammer. In this case, however, the response is measured with the dynamometer in order to capture the dynamics of its piezoelectric sensors in the FRF. Response data from the dynamometer passes through a Kistler type 5010 amplifier to a National Instruments compact (cDAQ-9171) data acquisition card, while the impact hammer (Kistler 9722A500) is connected directly to the DAQ card. The DAQ card in turn is connected to a VAIO laptop, running CutPro Software version 14.0.531 which is used to construct the frequency response function from the measurements.

3.1 System Identification

The system identification toolbox in MATLAB is used to fit a useful mathematical model to the measured FRFs. An initial 6-DOF relative degree one transfer function

H_{xx}						
i	1	2	3	4	5	6
a	3788	2.563E8	6.425E11	2.164E16	2.709E19	6.019E23
b	3566	8.364E7	7.676E11	1.432E16	3.933E19	6.0186E23
H_{yy}						
i	1	2	3	4	5	6
a	3308	2.383E8	5.580E11	1.624E16	1.934E19	3.376E23
b	2226	5.652E7	4.639E11	9.460E15	2.207E19	3.377E23
H_{zz}						
i	1	2	3	4	5	6
a	2788	3.308E8	5.375E11	3.324E16	2.087E19	9.319E23
b	6150	1.507E8	1.425E12	2.790E16	5.788E19	9.731E23

Table 3.1: Identified transfer function parameters of the dynamometer [16]

model of the form

$$H(s) = \frac{F_d(s)}{F_m(s)} = \frac{b_1 s^{n-1} + b_2 s^{n-2} + ... + b_n}{s^n + a_1 s^{n-1} + ... + a_n} \tag{3.1}$$

is obtained with the toolbox, and then the poles and zeros of the model are manually tuned to ensure that the model is minimum phase. This is done to ensure that the conditions for the SMO outlined in the previous chapter are satisfied. The fitted FRFs are shown in Fig.3.1 while the values of the numerical constants are given in in table3.1. The system identification toolbox quantifies the quality of the fit between the model output and measured data by calculating a normalized root mean square (NRMSE) fitness value, calculated as [15]

$$\text{fit } = 100\left(1 - \frac{\|y - \hat{y}\|}{\|y - \text{mean}(y)\|}\right) \tag{3.2}$$

and expressed as a percentage, where y is the validation (measured) data and $\hat{y}$ is the model output. In this definition, a higher fitness value corresponds to a higher quality fit. When the bandwidth over which the data is fitted is constrained with an upper limit of 1.6×10^4 rad/s ($\approx$ 2546 Hz), the NRMSE values for the transfer function models in X, Y, and Z direction are 91.00%, 85.98%, and 90.18%, respectively. The state-space model of the system in equation 2.1 is obtained by first mapping the coefficients identified in table3.1 to the canonical version of the state space model,

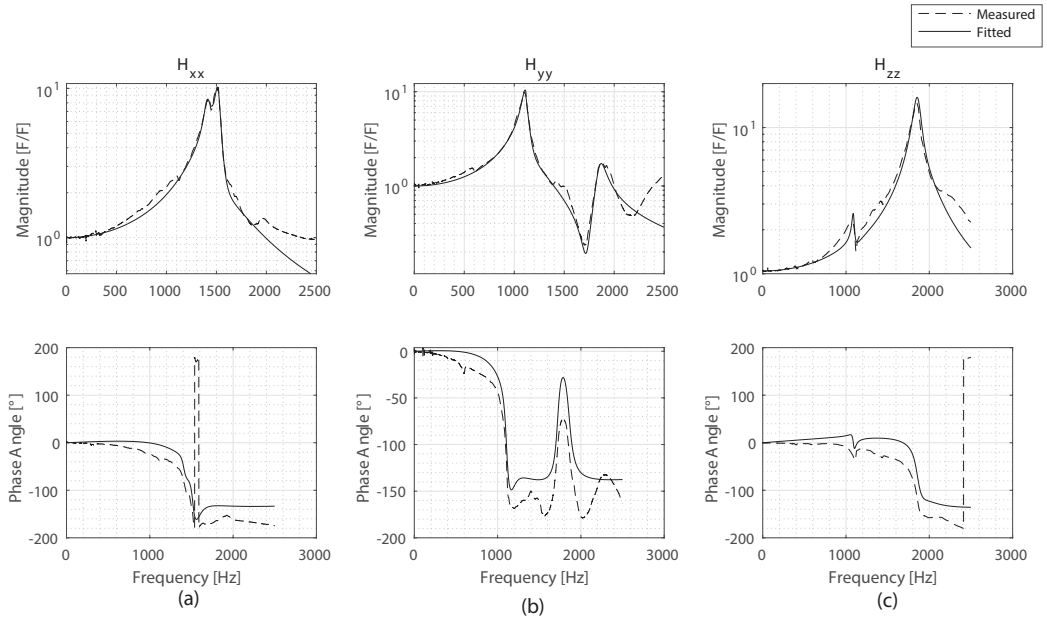

Figure 3.1: Measured and identified FRFs between applied and measured forces in the X (a), Y (b), and Z (c) directions of the dynamometer. The FRFs were measured after completing the last machining pass, as described in the experimental procedure of the cutting tests in chapter 4. The simulation study described in this chapter was conducted prior to the cutting tests described in chapter 4 to verify the force estimation methods of the previous chapter. The simulation study was then repeated with the FRFs identified during the experiment with machining forces consistent with the cutting conditions of the experiment so that a reasonable baseline with which to evaluate the experimental results is established. The results presented in this chapter are of the second, latter simulation.[16]

expressed as

$$\begin{aligned} \{\dot{x_c}(t)\} &= [A_c]\{x_c(t)\} + \{B_c\}F_m(t) \\ F_d(t) &= [C_c]\{x_c(t)\} \end{aligned} \tag{3.3}$$

where

$$[A_c] = \begin{bmatrix} -a_1 & -a_2 & ... & -a_n \\ 1 & 0 & 0 & 0 \\ \vdots & ... & ... & \vdots \\ 0 & ... & 1 & 0 \end{bmatrix}; \{B_c\} = \begin{Bmatrix} 1 \\ 0 \\ \vdots \\ 0 \end{Bmatrix}; [C_c] = \begin{bmatrix} b_1 \\ b_2 \\ \vdots \\ b_n \end{bmatrix}^T \tag{3.4}$$

Then equation 2.1 is obtained by applying the following similarity transforms to equation 3.3:

$$[A] = [T]\,[A_c]\,[T]^{-1}; \quad \{B\} = [T]\,\{B_c\}; \quad [C] = [T]^{-1}\,[C_c] \tag{3.5}$$

These transformations are applied to improve the condition number of the system matrix.

3.2 Simulated Cutting Conditions

CutPro software[17] is used to simulate the cutting forces in a milling process. CutPro is developed by MAL Inc., a company founded in 1996 that markets advanced manufacturing software developed by the Manufacturing Automation Laboratory at the University of British Columbia. Cutpro allows for the simulation of cutting forces regardless of the particular geometery of the tool. The general mechanics and dynamics models used in Cutpro were validated experimentally for helical endmills by Altintas and Lee[18]. The cutting conditions used in the simulation assume an aluminum workpiece, a two-flute end-mill with a diameter of 6.35 mm, a feed rate of 1000 mm/min, a spindle speed of 15345 rpm, and an axial depth of cut of 0.5 mm. The resulting cutting data represents the true cutting forces produced by the interaction of the tool and the workpiece, which is obtained over 60 seconds. This data is then imported into a purpose-made MATLAB script where it is distorted by additive white Gaussian noise and by the dynamics of the identified transfer function model. This process is repeated for simulated up- and down-milling at both full and half immersion cutting. The simulated cutting forces are then recovered by applying each of the three methods outlined in chapter 2. Selected results for each method are presented in the following sections.

3.3 Simulated AKF Results

As mentioned previously, the quality of the force reconstruction with AKF method depends on the value chosen for the regularizing factor S, as well as the values of R and Q. The standard Kalman filter effectively uses two sources of information, the process model and measurement updates, to estimate the unknown states of the system. Assigning a particular set of values to R and Q has the effect of prescribing a

weighting for the information obtained from the two sources. Theoretically, the values of the process and measurement covariance should be known, but Q can be tuned if the process uncertainty is not known [19]. For ease of analysis, each component of the state vector is assumed uncorrelated with each other and the corresponding covariance identical. Q then takes the form of a diagonal matrix with constant Q_0 defining each non-zero element of Q. Q_0 is set to zero because the uncertainty of the process is not known and the identified system models fit the measured FRFs exceptionally well.

The value of R is determined by adding Gaussian white noise to the simulated cutting forces, assuming an arbitrary signal to noise ratio (SNR), and then calculating the covariance of the perturbed signal. By design, the value of R is set equal to 0.02 N^2 by arbitrarily assuming an SNR of 17, and in this way the measurement covariance for the Y direction forces in the simulation study and the experimental cutting tests presented in chapter 4 are consistent with each other. The value of S, meanwhile, is tuned to strike an acceptable trade-off between the estimation error of the machining forces and the amount of noise introduced into the reconstructed signal. If S is too low, the regularizing factor does not sufficiently eliminate noise in the signal, but if the regularizing factor is too high, the noisy data will be excessively smoothed and the recovered signal distorted. The optimal value is obtained by plotting the smoothing and error norms for values of S in an interval of interest, which in this case is $10^{-5} \leq S \leq 10^5$. The smoothing norm is the norm of the estimated machining forces, and the error norm is the norm of the estimation error of the output (measured) forces. The optimal value of S is chosen as the value obtained at the knee of the curve for the error norm as shown in Fig3.2, so that the estimation error assumes a minimal value and the resulting estimation is not excessively smoothed.

While the value of Q, practically speaking, can be tuned when prior knowledge of the process covariance is lacking, the value of R must be precisely determined based on the known measurement process. The consequences for doing otherwise is illustrated in Fig.3.3. The figure shows the smoothing and error norms calculated for a wide combination of values for R and S, so that a 3D mesh plot of the smoothing and error norms is generated. The range of values considered are $[10^{-5}, 10^5]$ for both R and S. It is readily observed from the figure that for a given value of R a pair of smoothing and error norm curves as presented in Fig.3.2 is defined. Increasing or decreasing the value of R alters the shape of these curves so that an incorrect optimal value of S may

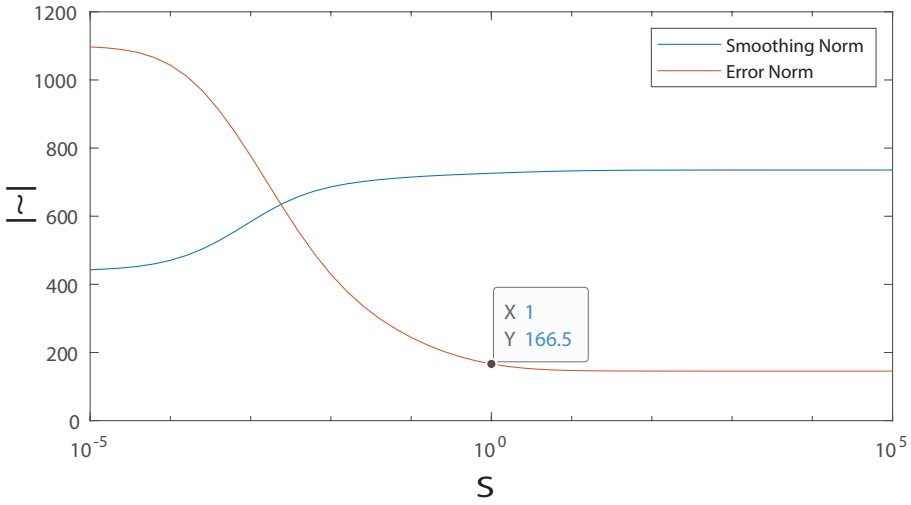

Figure 3.2: L-Curve for Hyy with Q = 0 and R = 0.02

be inferred. In other words, the value of R cannot be arbitrarily assigned or tuned because assuming a value of R that is inconsistent with the measurement system of a real, physical system would "bias" the resulting L-curve and a sub-optimal value of S chosen. With the values of S, R, and Q determined, the simulated cutting forces, which are perturbed by measurement noise and the dynamics associated with Hyy in the previous section, are reconstructed as shown in Fig.3.4. While only a short snapshot is given in the figure to improve visibility, the AKF consistently estimates the cutting forces over the entire time series of the simulation.

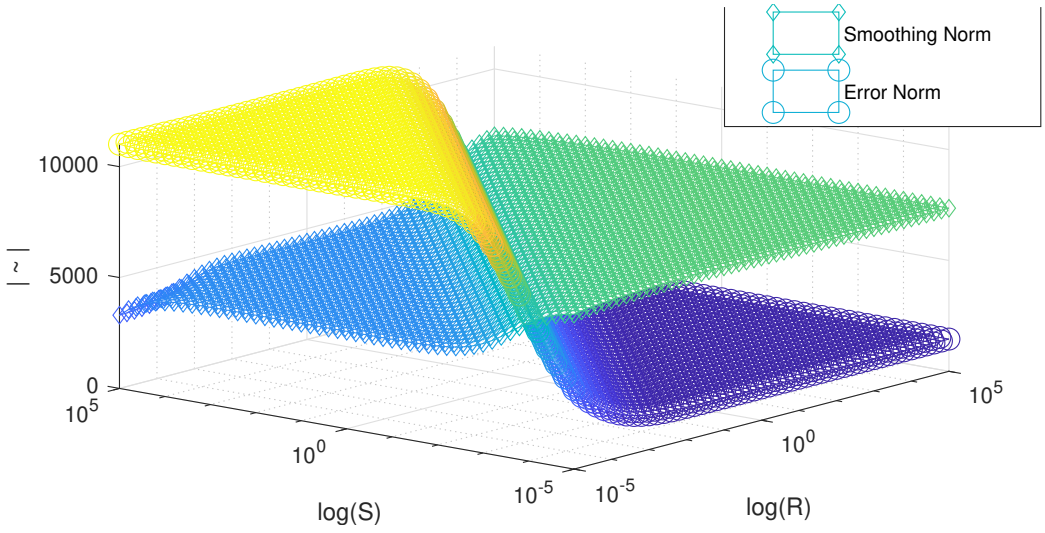

Figure 3.3: Error map for Hyy for different smoothing and measurement error norms

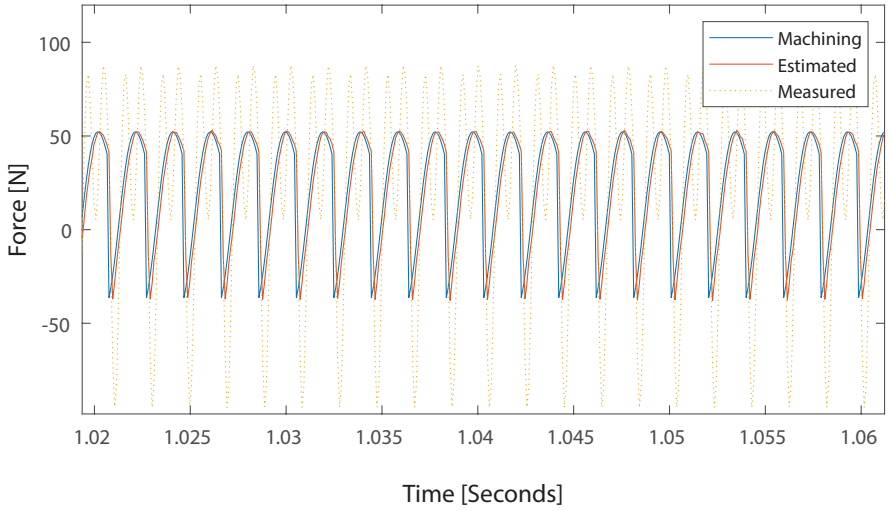

Figure 3.4: Simulated cutting forces reconstructed with Augmented Kalman Filter, where the cutting forces are distorted by the dynamics represented by Hyy

3.4 Simulated SMO Results

The observer in equation 2.12 is implemented in MATLAB and Simulink to recover the simulated cutting forces distorted by the same dynamics and measurement noise used in the previous section assuming the same SNR. The linear and non-linear gains are first calculated from equations 2.19 in MATLAB. The observer is then implemented and the machining forces recovered in the Simulink model shown in Fig.3.5. As is shown in the figure, the machining force and measurement noise are imported into the model as distinct time series, with the Machining Force signal distorted by the dynamometer dynamics before being perturbed by additive noise to produce the Measured Force signal. Here, the measurement noise signal is the same as that used for the AKF simulation in the previous section. The output vector of the observer is subtracted by the Measured Force to obtain the output estimation error, which is used to calculate the value of the smoothed switching function, where δ is set to 65 and ρ is tuned to a value on the order of 10^7 to ensure that the reachability condition of SMO is satisfied. Meanwhile, A^s_{22} is arbitrarily set equal to -1. The output of the switching function then combines with the output estimation error to form the input vector for the observer.

Meanwhile, the Compensated Force signal (reconstructed forces) is obtained from the switching function according to equation 2.22. Note that the switching function that is fed to the observer does not include the parameter $\mathcal{B}$. The Compensated, Measured, and Machining forces are shown in Fig.3.6. As was done in the previous section, 0.02 seconds of each of the time series is shown to improve the readability of the figure, although the observer consistently recovers the machining force for the entire time series. The time required for the observer to converge to sliding motion is on the order of milliseconds.

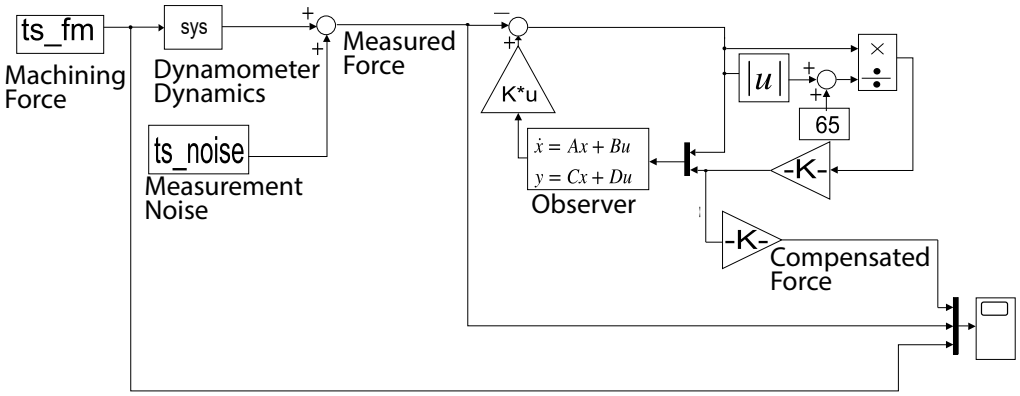

Figure 3.5: SMO block diagram in Simulink.

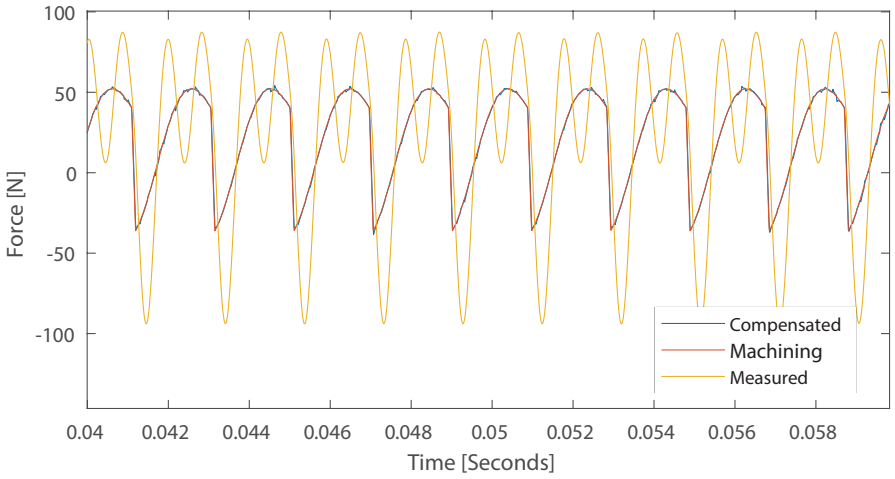

Figure 3.6: The cutting forces reconstructed by SMO compared with measured and true forces.

3.5 Simulated RD Results

In this method, equation 2.27 is used to recover the true machining forces from the simulated measurement signal after the impulse response of the system is obtained as outlined in section 2.3 Here, α is set equal to 0.3 and the machining force, measurement noise, and system dynamics are the same as those used in the previous sections. The method for choosing α is explained in detail in the next chapter. The resulting estimated force is shown in Fig.3.7 along with the machining and measured force signals. Unlike AKF and SMO, only a portion of the machining force signal (approximately 0.11 seconds or 1171 measurement samples) is recovered to circumvent the large computational cost associated with solving the inverse problem, and then 0.02 seconds of that portion is displayed for improved visibility.

As can be seen in the figure, a noticeable and disconcerting time delay on the order of half a millisecond is present between the actual (machining) and compensated (estimated) forces. This warrants some attention as this phenomenon does not appear to be present in the simulated results for either AKF or SMO and will be discussed further in the next chapter.

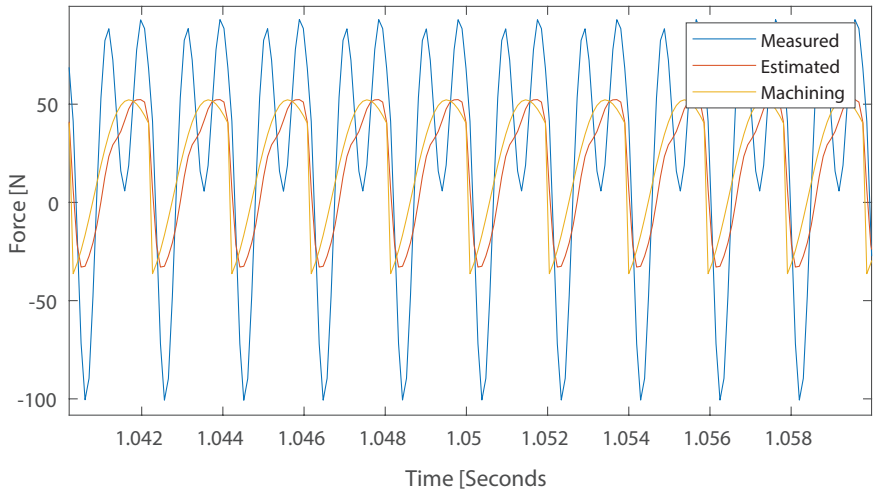

Figure 3.7: The cutting forces reconstructed by RD.

Chapter 4

Experimental Results

Some of the material presented in this chapter first appeared in "Measurement of high-frequency milling forces using piezoelectric dynamometers with dynamic compensation" Journal of Precision Engineering*, vol.66, pp.1-9,2020.*

With the methods outlined in chapter 2 verified in the previous chapter, they are then used to reconstruct the machining forces produced in an experimental cutting test.

4.1 Procedure

A custom workpiece with which to perform cutting tests is machined according to the dimensions in Fig.4.1. The workpiece is mounted onto the dynamometer via a custom mounting adapter plate while the dynamometer is fixed to a second plate connected to the bed of the computer numerical control (CNC) milling machine by T-bolts. The same arrangement of data acquisition equipment that was used to identify the transfer function models in Fig.3.1 is used to measure the machining forces with the dynamometer. A 6.35 mm diameter, two-fluted endmill is used to cut the Al 6061 workpiece at an axial depth of cut of 0.5 mm. Full immersion linear cuts in the X direction are made with a feed rate of 1000 mm/min and a spindle speed of 15,345 RPM. The spindle speed is chosen so that the harmonics of the tooth passing frequency coincide with the resonant peaks of the FRFs in the X and Y directions, which would result in the largest distortions of the machining forces possible in the forward transfer function. 9 trials are performed so that the height of

the workpiece is reduced from 25 to 20.5 mm. After each cutting pass, the dynamics of the dynamometer-workpiece assembly is measured using the same procedure for the hammer tests described in the previous chapter. In this way, the performance of the different force estimation methods can be evaluated as the dynamics of the assembly change. The force reconstruction methods outlined in chapter 2 are then used to recover the cutting forces in the distorted measurement.

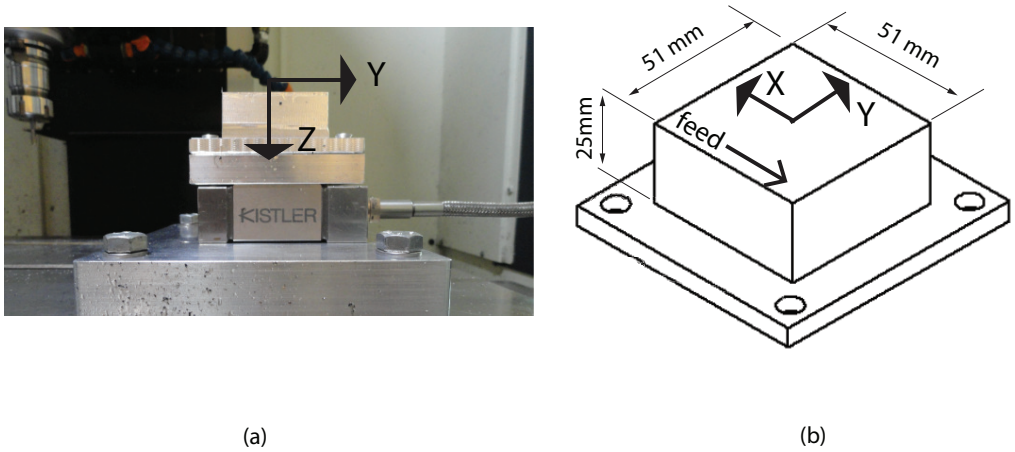

Figure 4.1: The experimental setup:(a) the workpiece and table dynamometer; (b) The dimensions of the workpiece. [16]

4.2 RD Results

As was the case for the simulation study, only a portion of the measurement data is used to recover the undistorted machining forces to keep the computational complexity low. Here, 0.95 seconds, or 6071 samples from the measurement signal, were used in the RD method. The measured forces and the resulting estimated forces for a 0.02 second period are presented in parts (a), (d), and (g) of Fig.4.2. As can be seen in the figure, the RD method is capable of correcting the exaggerated amplitudes caused by the resonant peaks of the dynamometer dynamics. The success of the method is confirmed by checking the fast Fourier transform (FFT) of the measured and reconstructed forces (parts (b), (e), and (h) of the same figure), where it is

observed that the presence of the second and third harmonics have been suppressed in the reconstructed forces in the Y and X directions, respectively. This is accomplished by selecting optimal values of α using the L-curve method as described by Jacquelin[10]. Analogous to how the regularizing factor S was determined for AKF, the L-curve method consists of plotting the smoothing norm against the error norm for a set of values for the regularizing factor, effectively creating a curve parameterized by α. Plotting the resulting curve on a log-log plot produces the characteristic "L-shape" of the curve. As was done for AKF simulation, the optimal value of α is the value corresponding to the "knee" of the curve, representing an ideal trade off between the smoothness of the reconstructed forces and the quality of the fit to the true signal. The L-curves for the cutting forces in the X, Y, and Z directions along with the respective optimal values of α are shown in parts (c), (f), and (i) of the figure. As can be seen from the figure, RD is successful in recovering the machining forces in all three directions; however, the reconstructed force in the Z direction is substantially more affected by noise due to the fact that the force component in that direction is significantly smaller, resulting in a much lower signal to noise ratio. For these reasons, the Z direction forces are neglected in the results in the subsequent sections.

4.3 AKF Results

The machining forces reconstructed with AKF are presented in Fig.4.3. The covariance of the measurement noise is obtained by observing the noise present while measurements are obtained during air cutting (when no contact is made between the tool and the workpiece and, therefore, the measured force is expected to be zero). In the X-direction R is 0.007 and in the Y-direction 0.02 N^2. Process noise Q_0 and regularization factor S are determined in the same manner as in the simulation study: process noise is assumed zero and the regularization factor is determined according to the error estimation curves in parts (e) and (f) in the figure. S is set to 0.01 and 0.1 in the X and Y-directions, respectively, after they are allowed to vary between 10^{-3} and 10^{-3}. As can be seen in parts (b) and (d), AKF is also successful in compensating for the harmonic components of the cutting forces in the reconstructed forces.

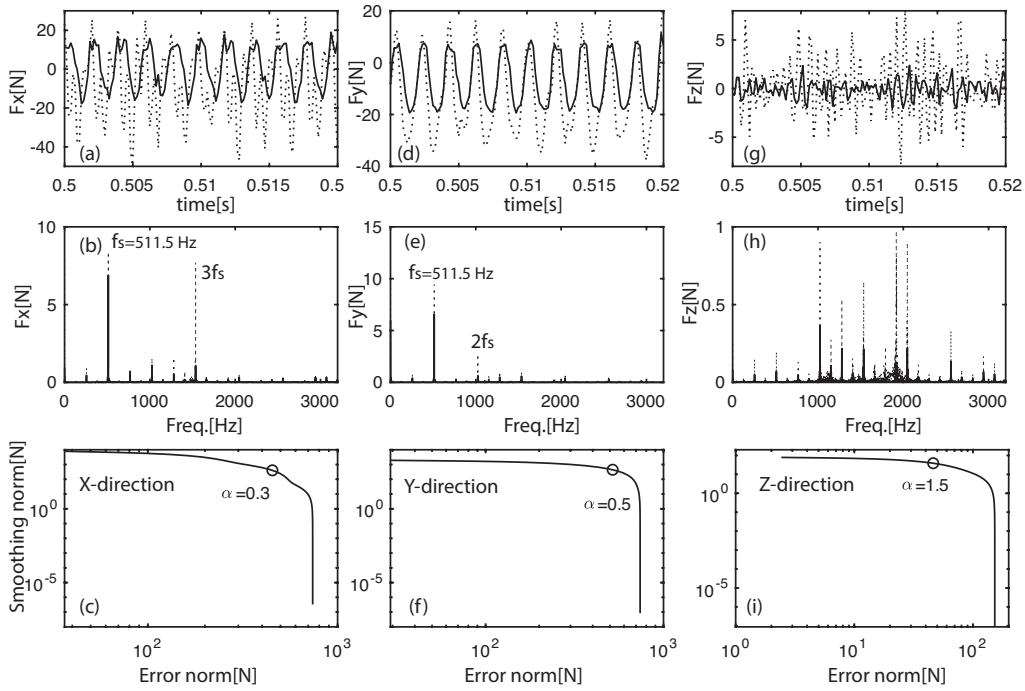

Figure 4.2: Reconstructed machining forces from dynamometer measurements using Regularized Deconvolution method. (a, d, g) measured and reconstructed forces in X, Y, and Z directions, (b, e, h) FFT of the measured and reconstructed forces, and (c, f, i) L-curves in X, Y, and Z directions. Measured forces are shown with dotted lines, and reconstructed forces are shown with solid lines. [16]

4.4 SMO Results

The machining forces recovered by SMO, which is implemented in the same manner as in the simulation study, are presented in Fig.4.4. The pole A^s_{22} is again set to -1 and the switching gain is $\rho = \max(\tilde{F}_d)|\mathcal{B}|$ to ensure that the sliding surface is reached. This is demonstrated in parts (e) and (f) of the figure: arbitrarily defined initial states of the observer produce large output estimation errors which quickly (in about 0.02 seconds) converge to zero as the sliding surface is reached. Sliding motion is maintained for the remainder of the cutting process. Again, the machining forces are recovered from the measurement signal (parts (a) and (c)) as the harmonics of the tooth passing frequency are suppressed in the reconstructed forces (parts (b) and (d)).

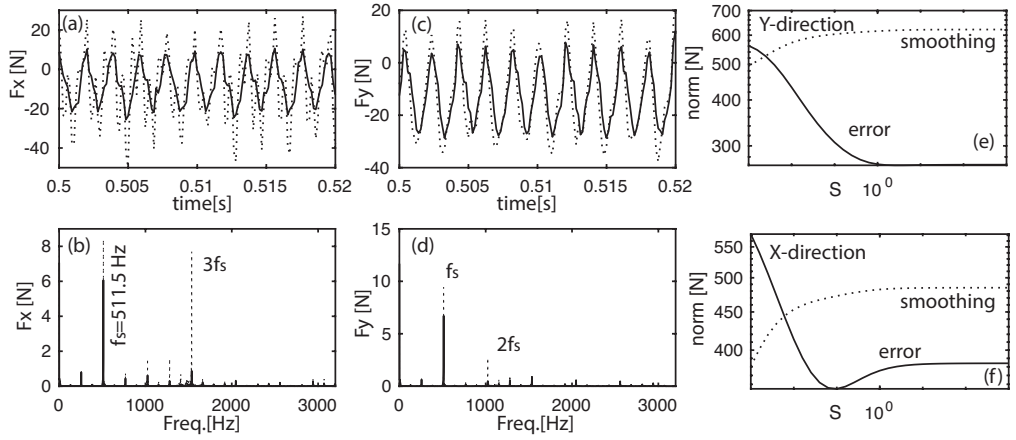

Figure 4.3: Reconstruction of machining forces from dynamometer measurements using Augmented Kalman Filter method. (a and c) measured and reconstructed forces in X and Y directions, (b and d) FFT of the measured reconstructed forces, and (e and f) variation of smoothing and output estimation error norms when regularization gain S varies between 10-3 and 10+3. Measured forces are shown with dotted lines and reconstructed forces are shown with solid lines.[16]

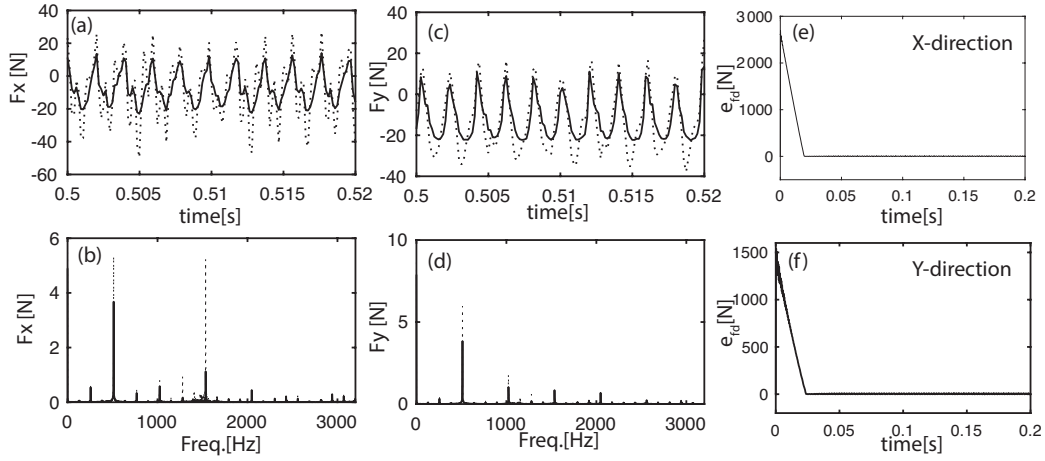

Figure 4.4: Reconstruction of the machining forces from dynamometer measurements using SMO method. (a and c) measured and reconstructed forces in X and Y directions, (b and d) FFT of the measured and reconstructed forces, and (e and f) variation of output estimation error. Measured forces are shown with dotted lines and reconstructed forces are shown with solid lines. [16]

4.5 Analysis

The machining forces reconstructed by RD, AKF, and SMO are presented in Fig.4.5. As was demonstrated in the previous sections, all three methods are capable of remov-

ing the effects of the harmonics of the tooth passing frequency from the measurement signal and recovering the expected cutting forces; however, as can be seen in the figure, slight variations persist between the machining forces reconstructed by each method, which is caused by differences in how each method works with the measurement signal and how this, in turn, affects the influence of the noise embedded in the measurement. Most notably, the time delay encountered during the simulation study of RD is present in the experimental results, particularly for the X-direction forces. In their work, Jacquelin et al. note that a time delay occurs in the response of the system when a "naive" solution (without regularization) to equation 2.25 is attempted due to the wave propagation time associated with the distance between the impact (input) force and the measured response when that distance is significant, and that such a delay is associated with rank deficiency and an under-determined solution to the inverse problem[10]. The motivation for regularization is, in part, to address this issue, so the fact that the time delay persists despite the use of the L-curve method suggests that the performance of RD is highly sensitive to the choice of α. Reducing the time delay in the cutting forces reconstructed by RD may require carefully iterating through a region of the L-curve representative of the knee or finding an optimal regularizing factor using a different method examined in Jacquelin's work, such as Generalized Cross-Validation. Moreover, the results provided by RD are affected by the fact that it minimizes the global estimation error instead of the error at the local time step[8][16] and that methods based on Tikonov regularization can be affected by increased ill-conditioning at resonance[8].

SMO and AKF, on the other hand, minimize the estimation error at each time step. Both of these methods produce similar results in Fig.4.5, but, as can be observed in Fig.4.6(a), there is a much larger output estimation error associated with AKF. As was demonstrated in section 2.2, sliding motion is reached, and therefore output estimation error converges, in finite time, whereas AKF only eliminates the error asymptotically, with the steady-state error directly influenced by the gains used to design the filter. These gains are coupled to the process and measurement noise of the system, while the performance of SMO is independent of such variations. This can be demonstrated by comparing the performance of the two methods at the start and the end of the experiment when SMO and AKF are each designed based on information obtained during the first machining pass. As can be seen by comparing Figs.4.4 and 4.6, SMO continues to perform as expected despite changes to the

system dynamics, which for example shifted the resonance peak in the Y-direction from 1020 Hz initially to 1110 Hz as shown in Fig.3.1 after the final cutting pass. It should be noted that the slight errors in Fig.4.6(a) are due in part to discretization. The susceptibility of AKF to these variations is shown in Fig.4.6(b), where it can be observed how the changing dynamics affect the variation of the smoothing and error norms with the parameter S after the AKF is initially designed. This supports the analysis in section 3.3, which asserts that the values of R and S must be determined with care to produce good results. Moreover, the influence of Q has not yet been considered as accurate knowledge of the process noise associated with the changing system dynamics can not be known prior to the experiment, limiting the accuracy of AKF.

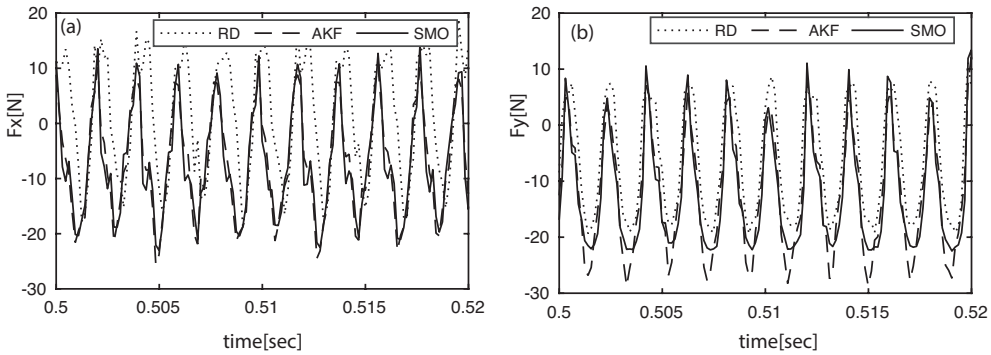

Figure 4.5: Comparison of the machining forces reconstructed dynamometer measurements using RD, AKF, and SMO methods. [16]

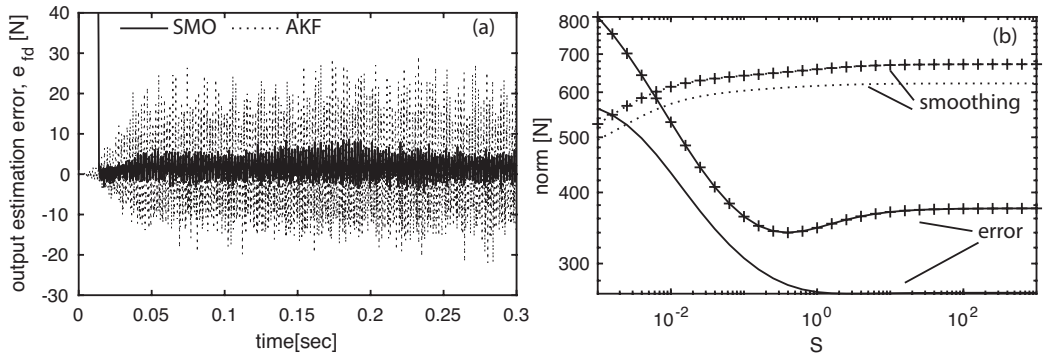

Figure 4.6: a) Output estimation error resulting from SMO and AKF methods applied on the normal forces measured during the first pass, and (b) variation of the smoothing and output estimation error norms when the regularization factor of AKF varies between $10^{-3} \leq S \leq 10^{3}$. + marker indicates the smoothing and estimation error norm plots when the forces during the first pass are used. [16]

Chapter 5

Conclusion

In this work, three methods to reconstruct milling forces that are distorted by the high-frequency dynamics of piezoelectric dynamometers were investigated. The theoretical background of RD, SMO, and AKF was presented and these were methods verified with a simulation study before being applied to recover the forces in a live cutting experiment that involved exciting the resonant frequencies of the dynamics of a piezoelectric dynamometer, that had previously been identified, with the harmonics of the tooth passing frequency of the cutting tool. The effectiveness of the three methods in removing the effects of these harmonics was evaluated and compared, as was their performance in the simulation study.

The results of this study showed that both AKF and SMO performed better than RD, primarily due to the fact that AKF and SMO minimized the output estimation error at each local timestep, whereas RD minimized the global estimation error. Between the two former methods, SMO proved to be more effective. This is due to the fact that SMO is able to eliminate output estimation errors in finite time and that its performance is robust against variable system structures. However, SMO does suffer from large initial errors, as was shown in Figs. 4.4(e) and (f) and 4.6(a), and is more sensitive to discretization. The latter is true because, unlike AKF and RD, SMO is formulated in the continuous time domain. Furthermore, the discretization associated with digital controllers and data acquisition adversely affects the frequency of the switching function due to sampling errors and as a result sliding motion cannot be guaranteed, necessitating research into a discrete-time domain implementation of SMO.[20] AKF, by contrast, has much lower estimation errors initially and is easily applied to discrete data, but is highly sensitive to the process and measurement

noise under consideration and performs poorly when the dynamics of the system change. RD, on the other hand, is not necessarily robust against changing dynamics, is highly sensitive to the choice of regularizing factor, and can not be used as an online method due to the computational complexity of solving the associated inverse problem. Moreover, the matrix $[G]$ can in some situations be ill-conditioned, especially when the resonance peaks of the system are excited. However, RD has the advantage of not requiring prior knowledge before being implemented, whereas even SMO requires the gain of the switching function to be tuned.

While important insights have been gained by this work, opportunities for further work have been identified and additional research topics remain:

- Despite the difficulties encountered when using RD, the prospect of using a method that requires a minimal amount of tuning remains intriguing. It may be interesting to investigate how RD can be adapted to become more suitable for online force estimation.

- Although it has been demonstrated that AKF and SMO are suitable for online force estimations, this work does not actually constitute an example of an online application. Further research involving the application of these methods for online force estimation during machining, and the required work to establish a physical feedback control system to make this research possible, would be very rewarding.

- While the merits of SMO have been demonstrated in this work, applying this method for networked control systems remains an open research topic[21]. It will become increasingly imperative to pursue this topic as Industry 4.0 continues to be adopted in manufacturing processes[22].

Chapter 6

Bibliography

[1] S. Y. Liang, R. L. Hecker, and R. G. Landers, "Machining process monitoring and control: the state-of-the-art," *J. Manuf. Sci. Eng.*, vol. 126, no. 2, pp. 297–310, 2004.

[2] M. Elbestawi, T. Papazafiriou, and R. Du, "In-process monitoring of tool wear in milling using cutting force signature," *International Journal of Machine Tools and Manufacture*, vol. 31, no. 1, pp. 55–73, 1991.

[3] R. Teti, K. Jemielniak, G. O'Donnell, and D. Dornfeld, "Advanced monitoring of machining operations," *CIRP annals*, vol. 59, no. 2, pp. 717–739, 2010.

[4] N. Tounsi and A. Otho, "Dynamometer performance modeling and experimental assessment," *J. Dyn. Sys., Meas., Control*, vol. 122, no. 3, pp. 477–482, 2000.

[5] L. R. Castro, P. Viéville, and P. Lipinski, "Correction of dynamic effects on force measurements made with piezoelectric dynamometers," *International Journal of Machine Tools and Manufacture*, vol. 46, no. 14, pp. 1707–1715, 2006.

[6] A. Alcocer, A. Robertsson, A. Valera, and R. Johansson, "Force estimation and control in robot manipulators," *IFAC Proceedings Volumes*, vol. 36, no. 17, pp. 55 – 60, 2003.

[7] A. Mohammadi, M. Tavakoli, H. Marquez, and F. Hashemzadeh, "Nonlinear disturbance observer design for robotic manipulators," *Control Engineering Practice*, vol. 21, no. 3, pp. 253 – 267, 2013.

[8] E. Lourens, E. Reynders, G. De Roeck, G. Degrande, and G. Lombaert, "An augmented kalman filter for force identification in structural dynamics," *Mechanical Systems and Signal Processing*, vol. 27, pp. 446–460, 2012.

[9] L. Chan, F. Naghdy, and D. Stirling, "Extended active observer for force estimation and disturbance rejection of robotic manipulators," *Robotics and Autonomous Systems*, vol. 61, no. 12, pp. 1277 – 1287, 2013.

[10] E. Jacquelin, A. Bennani, and P. Hamelin, "Force reconstruction: analysis and regularization of a deconvolution problem," *Journal of sound and vibration*, vol. 265, no. 1, pp. 81–107, 2003.

[11] F. Bai and C. Chew, "Muscle force estimation with surface emg during dynamic muscle contractions: A wavelet and ann based approach," in *2013 35th Annual International Conference of the IEEE Engineering in Medicine and Biology Society (EMBC)*, pp. 4589–4592, 2013.

[12] M. Mihoub, A. S. Nouri, and R. B. Abdennour, "A second order discrete sliding mode observer for the variable structure control of a semi-batch reactor," *Control Engineering Practice*, vol. 19, no. 10, pp. 1216 – 1222, 2011.

[13] R. Brown, P. Hwang, and a. O. M. C. Safari, *Introduction to Random Signals and Applied Kalman Filtering with Matlab Exercises, 4th Edition*. John Wiley & Sons, 2012.

[14] C. Edwards and S. Spurgeon, *Sliding mode control: theory and applications*. Crc Press, 1998.

[15] MathWorks Inc., "Compare identifed model output and measured output." `https://www.mathworks.com/help/ident/ref/compare.html`. Accessed: 2022-04-22.

[16] A. Jullien-Corrigan and K. Ahmadi, "Measurement of high-frequency milling forces using piezoelectric dynamometers with dynamic compensation," *Precision Engineering*, vol. 66, pp. 1–9, 2020.

[17] Manufacturing Automation Laboratory Inc., "Cutpro simulation software." `https://www.malinc.com/products/cutpro/`. Accessed: 2022-04-22.

[18] Y. Altintaş and P. Lee, "A general mechanics and dynamics model for helical end mills," *CIRP Annals*, vol. 45, no. 1, pp. 59–64, 1996.

[19] J. Chae and S. Park, "High frequency bandwidth measurements of micro cutting forces," *International Journal of Machine Tools and Manufacture*, vol. 47, no. 9, pp. 1433–1441, 2007.

[20] L. Wu, J. Liu, S. Vazquez, and S. K. Mazumder, "Sliding mode control in power converters and drives: A review," *IEEE/CAA Journal of Automatica Sinica*, vol. 9, no. 3, pp. 392–406, 2022.

[21] J. Hu, H. Zhang, H. Liu, and X. Yu, "A survey on sliding mode control for networked control systems," *International Journal of Systems Science*, vol. 52, no. 6, pp. 1129–1147, 2021.

[22] M. Kuntoğlu, E. Salur, M. K. Gupta, M. Sarıkaya, and D. Y. Pimenov, "A state-of-the-art review on sensors and signal processing systems in mechanical machining processes," *The International Journal of Advanced Manufacturing Technology*, vol. 116, no. 9, pp. 2711–2735, 2021.